Study of charm hadronization and in-medium modification at the Electron-ion Collider in China

Senjie Zhu,[1,*] Xiao Huang,[1] Lei Xia,[1] Aiqiang Guo,[2,3] Yutie Liang,[2,3,4] Yifei Zhang,[1,†] and Yuxiang Zhao[2,5,3,6]

[1]*University of Science and Technology of China, Hefei, Anhui Province 230026, China*
[2]*Institute of Modern Physics, Chinese Academy of Sciences, Lanzhou, Gansu Province 730000, China*
[3]*University of Chinese Academy of Sciences, Beijing 100049, China*
[4]*Guangdong Provincial Key Laboratory of Nuclear Science, Institute of Quantum Matter, South China Normal University, Guangzhou 510006, China*
[5]*Southern Center for Nuclear-Science Theory (SCNT), Institute of Modern Physics, Chinese Academy of Sciences, Huizhou, Guangdong Province 516000, China*
[6]*Key Laboratory of Quark and Lepton Physics (MOE) and Institute of Particle Physics, Central China Normal University, Wuhan 430079, China*

(Received 20 October 2023; accepted 5 January 2024; published 23 January 2024)

Charm quark production and its hadronization in ep and eA collisions at the future Electron-ion Collider in China (EicC) will help us understand the quark/gluon fragmentation processes and the hadronization mechanisms in the nuclear medium, especially within a poorly constrained kinematic region ($x < 0.1$). In this paper, we report a study on the production of charmed hadrons, D^0 and Λ_c^+, reconstructed with a dedicated Geant4 simulation of vertex and tracking detectors designed for EicC. The Λ_c^+/D^0 ratios as functions of multiplicity and p_T, as well as the D^0 double ratio are presented with projected statistical precision.

DOI: 10.1103/PhysRevD.109.014029

I. INTRODUCTION

Exploring the most fundamental building blocks of the Universe is the paramount objective of modern physics. Over the past five decades, we have come to understand that matter, in its essence, is composed of nuclei and nucleons. These, in turn, are made up of even more basic components known as quarks, which are confined in a colorless bound state through the exchange of gluons. This interaction among quarks and gluons is governed by the theory of strong force, known as quantum chromodynamics (QCD). However, up to now, the constituent interactions and the dynamical distributions of quarks and gluons inside nucleons, in particular in the kinematic regime dominated by sea quarks and gluons, are still unclear or poorly constrained by existing experiments [1,2]. The next-generation experimental facilities with electron-ion collision have been proposed for the quantitative study of matter in this new regime, such as Electron-ion Collider at BNL (EIC-BNL) [3,4] and Electron-ion collider in China (EicC) [5].

EicC is proposed to operate at a center-of-mass (c.m.) energy ranging from 15 GeV to 20 GeV, with a luminosity of approximately $2.0 \times 10^{33}\ \mathrm{cm}^{-2} \cdot \mathrm{s}^{-1}$ [5]. This would enable EicC to explore the kinematic region dominated by sea quarks, effectively bridging the gap between the EIC-BNL and JLab 12 GeV (and a possible 24 GeV upgrade) experiments [5,6]. The primary objective of EicC is to delve into the partonic structure and three-dimensional tomography of nucleons and nuclei, the cold nuclear matter effects, as well as the origin of proton mass. This ambitious endeavor aims to significantly advance our understanding of these fundamental aspects of nuclear physics.

Understanding the interactions of partons with nuclear matter, as well as their fragmentation [7] or combination [8] to form hadrons—a process known as hadronization—is a fundamental question that future EicC experiments aim to answer. Heavy quarks, due to their large masses, are predominantly produced in the initial hard scatterings of collisions and undergo the complete evolution of the nuclear medium system. This makes them an ideal probe for measuring nuclear medium effects and heavy quark hadronizations in high-energy heavy-ion collisions [9–11].

For example, the enhancement of Λ_c^+/D^0 ratios in heavy-ion collisions compared with elementary particle collisions has been measured by STAR [10] and ALICE [12,13], revealing the hadronization mechanism of charm quark with light quarks in hot [8,14] and dense medium [15]. However, in these collisions, it is a complex task to separate the effect of the cold nuclear medium (CNM) from the dominant medium response caused by the hot quark-gluon plasma (QGP). This is where electron-ion

[*]zhusenjie@mail.ustc.edu.cn
[†]ephy@ustc.edu.cn

collisions come into play, offering an ideal platform to study the CNM effects [16] in a more transparent system, where it is believed no QGP is formed [17–19]. Moreover, two theories with different time scales—parton energy loss and the hadron absorption model [20]—can successfully describe the suppression of light hadrons in electron-ion collisions. The measurement of heavy quark production presents a novel opportunity to reveal the mechanisms of hadronization. To address these inquiries, it is essential to investigate charm hadronization and the production of open charmed hadrons in future EicC experiments.

In this paper, we perform a comprehensive simulation study with a Geant4 [21] detector configuration for open charm hadron production. The report is organized as follows. Section II introduces the simulation setup and process. Section III presents the simulation results, and a summary is given in Sec. IV.

II. SIMULATION SETUP

This study employs the PYTHIA event generator, as referenced in [22]. Two distinct versions of this generator, namely pythiaeRHIC (PYTHIA 6.4) and PYTHIA 8.3, are utilized in our analysis. The configuration for PYTHIA 6.4 is detailed extensively in Ref. [23]. The physical processes including vector-meson diffractive and resolved processes, semihard QCD $2 \rightarrow 2$ scattering, neutral boson scattering off heavy quarks within the proton, and photon-gluon fusion, are turned on. Several alternative hadronization models in PYTHIA 8.3 are used for charm hadronization studies, e.g., implemented color reconnection models. The kinematic variables used are listed in Table I.

The kinematic coverage of the collision with electron (3.5 GeV) and proton (20 GeV) is shown in Fig. 1 (top panel), which presents the $\log_{10}(x_B) - \log_{10}(\mathrm{Q}^2)$ distribution of charmed events per 1 fb^{-1} integral luminosity. As shown in the $x_B - Q^2$ distribution, one step along Q^2 distribution exists at $\log_{10}(Q^2) = 0.4$. The reason is that the subprocess cross section ($\gamma^* q \rightarrow q$) in PYTHIA 6 is deliberately set to zero when the photon's virtuality Q^2 approaches zero. This is done to prevent double counting with real-photon physics processes [22]. In the above beam setting and with DIS requirement $Q^2 > 1$ GeV^2, the x_B distributions are shown in the bottom panel of Fig. 1, including inclusive DIS events and charmed events. Charmed events account for 1.4% of inclusive DIS events. The momentum-θ phase space 2-dimension distribution of D^0 is shown in Fig. 2 (the first panel). Due to the higher momentum of the beam protons compared to the beam electron, the $D^0/\overline{D^0}$ distribution is skewed towards the direction of the proton beam. Consequently, as illustrated in

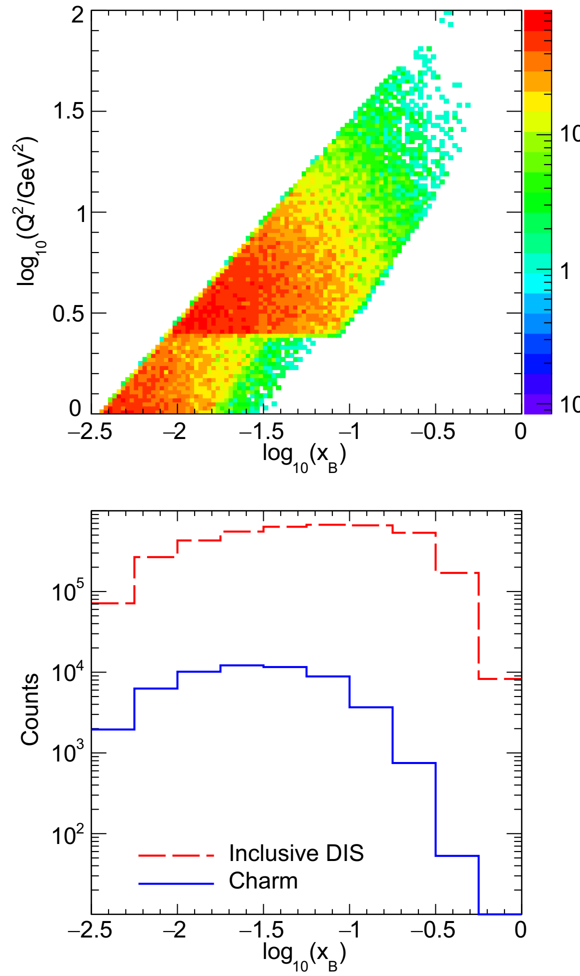

FIG. 1. (Top) $\log_{10}(x_B) - \log_{10}(Q^2/\mathrm{GeV}^2)$ distribution of charmed events per 1 fb^{-1}. (Bottom) $\log_{10}(x_B)$ distribution of inclusive DIS and charm per 1 fb^{-1} ($\mathrm{Q}^2 > 1$ GeV^2).

TABLE I. Kinematic variable definition.

k and k'	The four-momentum of the incoming electron and the scattered electron
p and p_h	The four-momentum of the incoming proton and the produced hadron
$q = k - k'$	The four-momentum of emitted virtual photon
$Q^2 = -q^2$	The negative square invariant momentum transfer of emitted virtual photon
$x_B = Q^2/(2p \cdot q)$	Bjorken scaling variable
$y = p \cdot q/(p \cdot k)$	The fraction of the incoming electron's energy transferred to the hadronic system
$z = p \cdot p_h/(p \cdot q)$	The momentum fraction of the virtual photon to be carried by the produced hadron
$W = \sqrt{(q+p)^2}$	The center-of-mass energy of γ^*-nucleon system
$\nu = q \cdot p/m_N$	The energy of γ^* in nucleon rest frame (m_N is the mass of the nucleon)

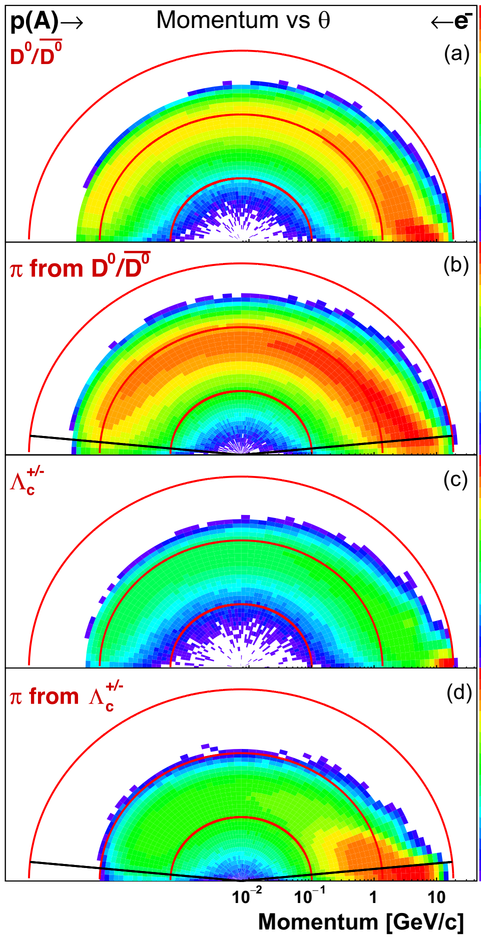

FIG. 2. The momentum-θ distributions of the particles produced by PYTHIA. The particle types are labeled respectively in the panel for $D^0/\overline{D^0}$, $\Lambda_c^{\pm}$ and pions from their decay.

the second panel of Fig. 2, the pions from $D^0 \to \pi K$ decay are given a boost, causing them to be produced more in the forward direction of the proton beam. As illustrated in Fig. 2 for $\Lambda_c^{\pm}$, the distributions of $\Lambda_c^{\pm}$ and the pions from its decay are even more skewed towards the direction of the proton beam. There is a region near $\theta = 0$, where the number of $\Lambda_c^{\pm}$ is significantly larger than in other areas, and the $\Lambda_c^{\pm}$ in this region has much higher energy. Furthermore, Λ_c^{+} is much more abundant than Λ_c^{-} in this region. This phenomenon is caused by the formation of beam remnants [24], a charm quark produced via the hard scattering, and u, d quarks from the beam proton form a Λ_c^{+} together. Because the u, d quarks from protons carry a large fraction of the proton momentum, the beam remnant Λ_c^{+} is very energetic.

The specific design and layout for EicC detectors have been detailed in Ref. [25], which include a tracking and vertex detector system. This report primarily focuses on the tracking and vertex detectors. The detector acceptance is $-3 < \eta < 3$ $(5.7° \sim 174.3°)$. In Fig. 2 [panels 2(b) and 2(c)], the acceptance region is marked by two black lines. In Ref. [25], the performances have been obtained through Geant4 simulation for different particle species (e, μ, π, K, p) under a 1.5T magnetic field configuration.

The performances for π are shown as an example in Fig. 3. In this study, the distance of the closest approach (DCA) are defined as the closest distance between the reconstructed track and the primary vertex in $r\phi$ plane ($\mathrm{DCA}_{r\phi}$) and z axis (DCA_z). The tracking efficiency, the momentum resolution, the DCA_z, and $\mathrm{DCA}_{r\phi}$ resolutions are shown in panels 3(a), 3(b), 3(c), and 3(d), respectively. In the absence of particle identification (PID) detector in the simulation, a 3σ separation power for PID is assumed in the prospected PID detector acceptance coverage listed in Table II. It is applied as a momentum hard cutoff as a function of η.

All the performance parameters mentioned above have been used to conduct a fast simulation for the physical projection. In this simulation, the track information generated by PYTHIA is adjusted, or "smeared," according to a Gaussian function to mimic the limitations of the detection capability. The number of the tracks in the acceptance ($-3 < \eta < 3$) and passing the tracking efficiency filters is used to determine the primary vertex resolution, which is

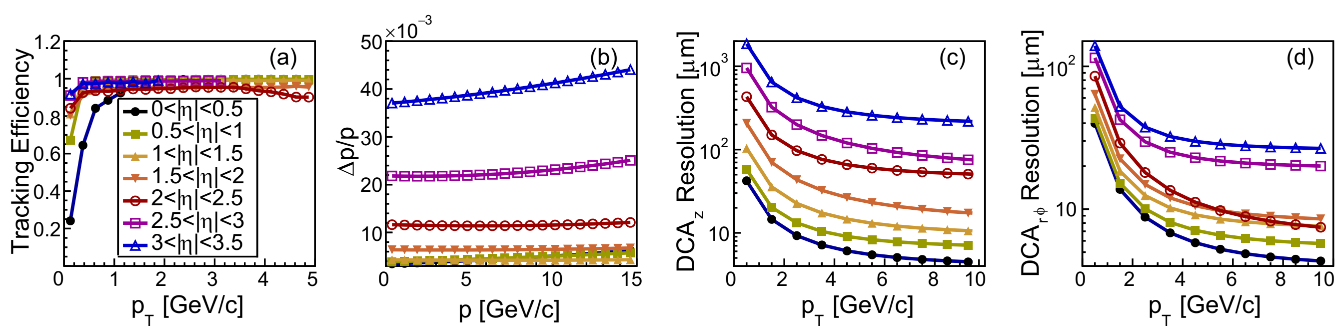

FIG. 3. The detector's performance for π: (a) the efficiency of track reconstruction, (b) the resolution of the reconstructed track momentum, (c) the resolution of the reconstructed track DCA in z direction, (d) the resolution of the reconstructed track DCA in the $r\phi$ plane. The different marker styles and line colors of the lines represent the different η regions of π, which are shown in the legend of the panel (a).

TABLE II. PID acceptance for hadrons at different η regions.

η	$[-3,-1)$	$[-1,1)$	$(1, 3]$
$p_{\max}$[GeV/c]	4	6	15

also smeared in the PYTHIA events. After smearing, different topological requirements are used to separate the signal and background.

D^0 is reconstructed from channel $D^0 \to \pi^+K^-$ with a branch ratio ($\mathcal{B}$) of 3.83% and Λ_c^+ is reconstructed from channel $\Lambda_c^+ \to \pi^+K^-p$ ($\mathcal{B} = 2.96\%$ in PYTHIA 6.4 and $\mathcal{B} = 3.4\%$ in PYTHIA 8.3). The $\mathcal{B}$ difference of Λ_c^+ between PYTHIA 6.4 and PYTHIA 8.3 is caused by a missing channel in PYTHIA 6.4 ($\Lambda_c^+ \to \Lambda\pi^+, \Lambda \to pK^-$). In the following part of this report, we use D^0 to represent both D^0 and $\overline{D^0}$ and use Λ_c^+ to represent both Λ_c^+ and Λ_c^-. In Fig. 4, we show topological cut diagrams for D^0 (a) and for Λ_c^+ (b). For D^0, three topological requirements are applied, including $\mathrm{DCA}_{\pi K}$, $\mathrm{Decay}L_{XY}^{D^0}$ and $\cos\theta_{XY}$, which are defined as

(i) $\mathrm{DCA}_{\pi K}$ is the closest distance between two daughter tracks.

(ii) $\mathrm{Decay}L_{XY}^{D^0}$ is the distance between the decay vertex and the reconstructed primary vertex (in the xy plane). Once $\mathrm{DCA}_{\pi K}$ is defined, two points that symbolize $\mathrm{DCA}_{\pi K}$ on each of the two tracks can be found. Then, the decay vertex of D^0 is defined as the middle of the two points.

(iii) $\cos\theta_{XY}$ is the cosine value of the angle between the D^0 decay length and the D^0 momentum (in the xy plane).

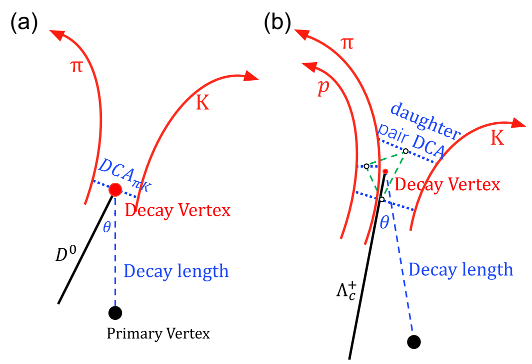

FIG. 4. Topological cuts applied to reconstruct D^0 (a) and Λ_c^+ (b).

The reason for defining both $\cos\theta_{XY}$ and $\mathrm{Decay}L_{XY}^{D^0}$ in the xy plane is that the spatial resolution in the xy plane is much better than that in the z dimension, especially in the end cap region. However, if the projections of two nonparallel lines in xy plane cross, $\mathrm{DCA}_{\pi K}$ will always be zero in the xy plane. Therefore, $\mathrm{DCA}_{\pi K}$ is defined in three dimensions instead of xy plane. For Λ_c^+, the $\mathrm{DCA}_{\pi K}$ is replaced by $\mathrm{DCA}_{\mathrm{daughters}}^{\max}$, the maximum of all three $\mathrm{DCA}_{\mathrm{daughters}}$, where $\mathrm{DCA}_{\mathrm{daughters}}$ is the DCA between two of the three daughters. The decay vertex is the center of all three decay vertexes defined by each daughter pair. All three topological cut distributions are shown in Fig. 5 for the signal (blue dashed line) and background (red solid line).

The πK invariant mass distributions in the D^0 mass region are fitted with a Gaussian function for signal and a linear function for background to obtain the D^0 signal yield. The significance is defined as $S/\sqrt{S+B}$, where S and B stand for the counts of D^0 signal and background, respectively. All the criteria are optimized by maximizing the significance iteratively. Figure 6 shows D^0 significance as a function of all three topological requirements. The optimal topological criteria are: (i) $\mathrm{DCA}_{\pi K} < 110$ μm, (ii) $\cos\theta_{XY} > -0.75$. As seen in Fig. 2 (the first panel), the p_T of most D^0 is lower than 1 GeV/c and D^0 with lower p_T tends to have a smaller $\mathrm{Decay}L_{XY}^{D^0}$, so the $\mathrm{Decay}L_{XY}^{D^0}$ distribution of signal is similar to that of background. Therefore, the significance is insensitive to $\mathrm{Decay}L_{XY}^{D^0}$ as shown in Fig. 6. In addition, the DCA between daughters and the primary vertex is not effective because the spatial resolutions of the detectors become worse when the curvatures of tracks are large at low p_T region.

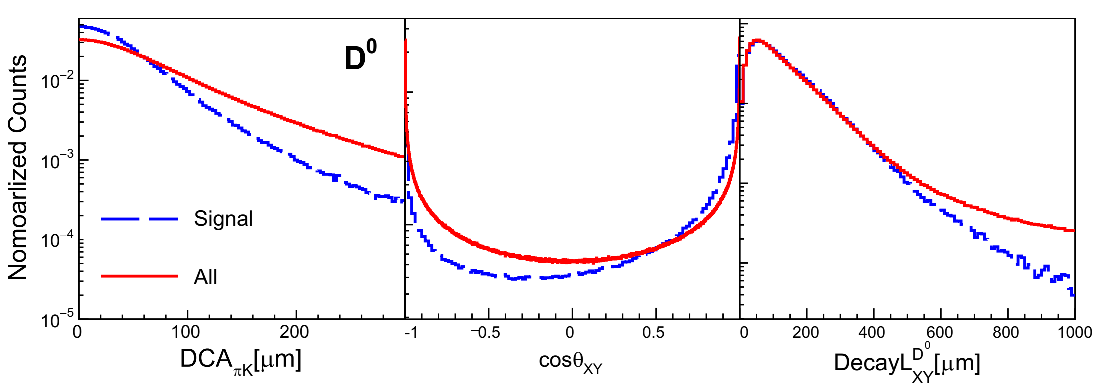

FIG. 5. Normalized D^0 topological cut distributions, where the blue lines are for signal and the red lines are for background.

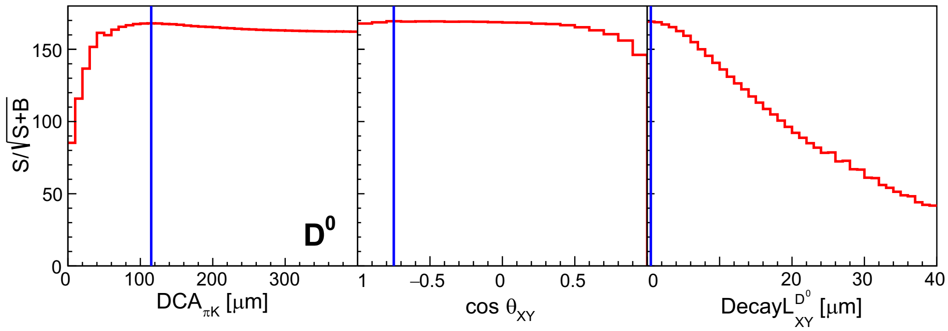

FIG. 6. Topological requirements are optimized to ensure the highest significance of D^0. The previous best results are applied to the next round of optimization.

The πK invariant mass distributions with different detector performance configurations are shown in Fig. 7. There are three configurations included: *no PID*, *with PID*, and **PID + Vertex**. In the first two configurations, the vertex detectors in the geometry for Geant4 simulation are removed to determine the significance of the vertex detectors in D^0 reconstruction. For *no PID*, the PID acceptance in Table II is not applied, and all possible combinations formed by particles with opposite charges are considered. As shown in Fig. 7, the signal peak of the green line (*no PID*) is almost invisible. Compared to the green line (*no PID*), the background of the blue line (*with PID*) is greatly suppressed when the PID acceptance is applied. Similarly, compared to the green line (*no PID*), the background of the red line (**PID + Vertex**) is also suppressed, and the mass peak is narrowed. This is because the momentum resolution becomes better when the vertex detectors are installed. After adding the vertex detectors, the significance improves from 13.9 to 21.8.

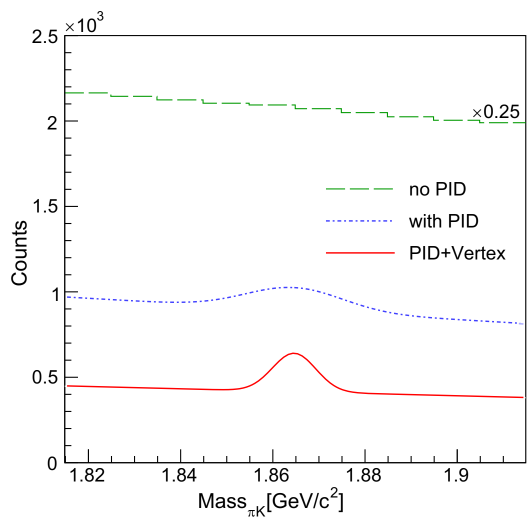

FIG. 7. The πK invariant mass distributions with different detector performance configurations:(*no PID*) without either PID system or vertex detectors, (*with PID*) with the PID system but without vertex detectors, (**PID + Vertex**) with the PID system and the vertex detectors. The significance is achieved at an integrated luminosity 0.04 fb^{-1}. The significances of *with PID* and **PID + Vertex** are 13.9 and 21.8, respectively. The S/B of *with PID* and **PID + Vertex** are 0.06 and 0.215, respectively. The distribution of *no PID* has been scaled by a factor 0.25 for clarity.

The reconstruction procedure is also carried out for Λ_c^+. The difference is that the shape of the Λ_c^+ peak is non-Gaussian, as shown in the bottom panel of Fig. 9. Therefore, we use the line shape of Λ_c^+ after smearing the daughter tracks from pure Λ_c^+ and a linear function in the fit. The distributions of Λ_c^+ topological cuts are shown in Fig. 8, where we can find that $DCA_{daughters}^{max}$ is the only useful criterion. Therefore, in Fig. 9, only the criterion optimization for $DCA_{daughters}^{max}$ is performed, and the optimal result is $DCA_{daughters}^{max} < 1000$ μm. The significance is improved from 34 to 38 with this requirement.

III. RESULTS

A. Baryon-to-meson ratios

The fragmentation ratios of the charm quark obtained from different experiments were thought to be universal. Both HERA ep collision measurements [26,27] and the previous pp collision measurements at LHC [28] are consistent with e^+e^- collision measurements [29]. However, an enhancement of Λ_c^+/D^0 ratio has been observed in the recent measurement at ALICE [12,30]. The deviation of the Λ_c^+/D^0 ratio from pp collision to e^+e^- collision experiment indicates that even a small hadronic system can affect charm hadronization. Therefore, the Λ_c^+/D^0 ratio should be reexamined in the ep collision system, specifically at EicC, which provides unique kinematic coverage and high luminosity.

Two projections of Λ_c^+/D^0 ratios are provided in this subsection. ep collision data with beam energies 3.5 GeV × 20 GeV are generated by PYTHIA 8.3 with QCD color reconnection (QCD-CR) tuning [31] and multiple-parton-interaction color reconncetion (MPI-CR) tuning [24]. Two color reconnection models are selected here because one tuning with color reconnection agrees with the enhanced

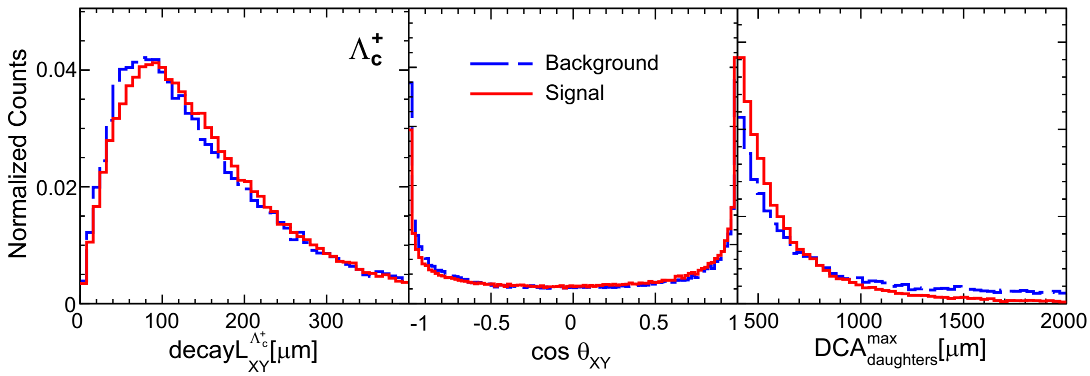

FIG. 8. Λ_c^+ topological cut distributions. The blue dashed and red solid lines represent the distributions for the background and signal, respectively. Because the differences of decay$L_{XY}^{\Lambda_c^+}$ and $\cos\theta_{XY}$ distribution between signal and background are small, $\mathrm{DCA}^{\mathrm{max}}_{\mathrm{Daughters}}$ is the only topological requirement taken into account.

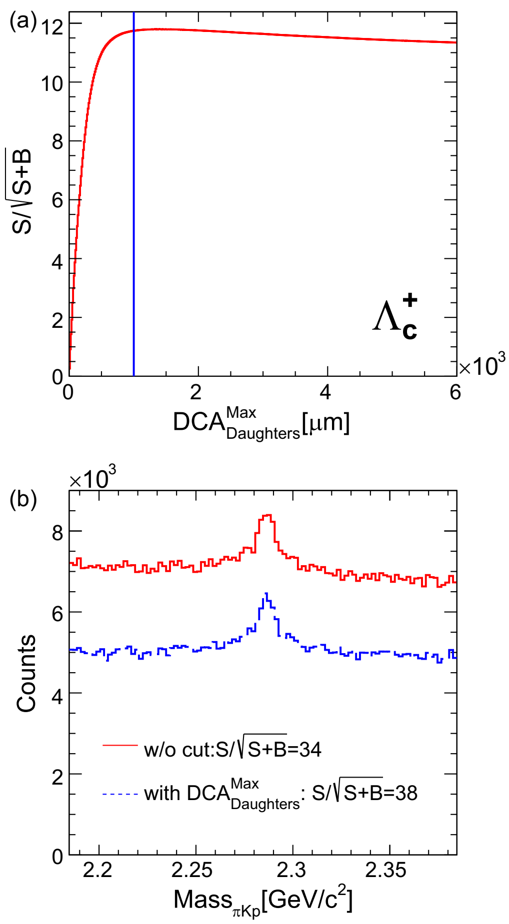

FIG. 9. The results of Λ_c^+ reconstruction. (a) the significance scanning for $\mathrm{DCA}^{\mathrm{max}}_{\mathrm{Daughters}}$. (b) the $\pi K p$ invariant mass distributions. The read solid and blue dashed lines represent the distributions without and with requirement application, respectively.

Λ_c^+/D^0 ratio at pp collisions in Ref. [32]. In Fig. 10, the statistical uncertainty projection as a function of p_T is shown. The curves are from PYTHIA 8.3, in which the solid and dashed curves are from the QCD-CR and MPI-CR

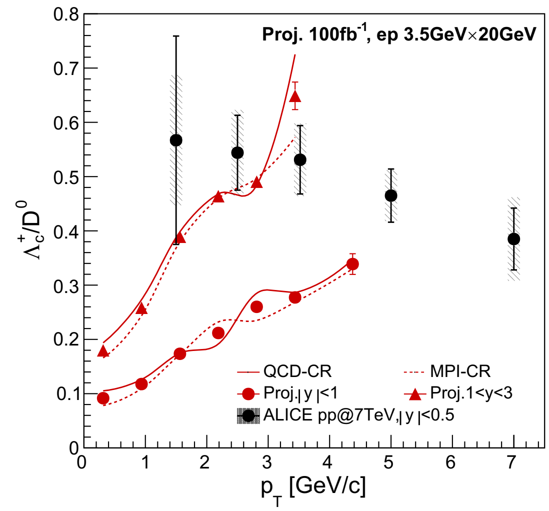

FIG. 10. The values of the red dashed and red solid lines are calculated from PYTHIA 8.3 with QCD-CR and MPI-CR. The red solid triangles and circles are the centers between the curves of the two models at both mid and forward rapidity. The red error bars represent the projection of Λ_c^+/D^0 ratio statistical uncertainties at an integrated luminosity 100 fb^{-1}. The black points are the result of ALICE measurement where the error bars are statistical uncertainties and the gray boxes are the systematic uncertainties [12].

settings. The values of the red points are the average of the two models at the corresponding rapidity regions. The estimation of statistical uncertainties is the root mean square of the sum of squares of errors propagated from all sources. For Λ_c^+/D^0 ratio, the expression is

$$\sigma\left(\frac{\Lambda_c^+}{D^0}\right) = \sqrt{\left(\frac{\sigma(\Lambda_c^+)}{N_{D^0}}\right)^2 + \left(\frac{N_{\Lambda_c^+}}{N_{D^0}^2}\sigma(D^0)\right)^2},$$

where the statistical uncertainties of D^0 and Λ_c^+($\sigma(D^0)$ and $\sigma(\Lambda_c^+)$) are calculated by the signal yields divided by the corresponding significance. The statistical uncertainty is scaled to an integral luminosity 100 fb^{-1}. The results of Λ_c^+/D^0 ratios are presented in two rapidity regions, the mid-rapidity region ($|y| < 1$) and forward-rapidity region ($1 < y < 3$), shown as solid circles and triangles, respectively. The measurement in the pp collision from ALICE [12] is also presented, and shown as black solid circles in Fig. 10. The black points represent the center values, the black line is the statistical uncertainty, and the gray box is the systematic uncertainty. Compared to ALICE, the statistical precision is significantly improved in EicC due to high luminosity and much less hadronic combinatorial background. EicC results show that the uncertainties are smaller than the difference between the two models at both mid and forward rapidity. This suggests that EicC has sufficient power to distinguish between different hadronization models. In addition, the Λ_c^+/D^0 ratios have different behaviors in mid- and forward-rapidity regions. A wide rapidity coverage, benefiting from large acceptance of the detector design, can be achieved at EicC. As mentioned above, there is an enhancement of Λ_c^+ production caused by beam remnant formation in the very forward rapidity region. With wider rapidity coverage of EicC, the interaction between beam remnant and charm quark can also be studied in greater detail.

Figure 11 shows the statistical uncertainty projections of Λ_c^+/D^0 as a function of charged particle multiplicity by red marks. The high multiplicity results from EIC-BNL simulation [33] are shown as the open blue marks. Only the tracks in $|\eta| < 3$, $p_T > 0.2$ GeV$/c$ and not from D^0 or Λ_c^+ decay are counted in the number of charge tracks. The dashed and solid lines are from the calculation of MPI-CR and QCD-CR PYTHIA 8.3 models, respectively. The red and blue curves are the results for EicC and EIC-BNL, respectively. EicC can provide a measurement of Λ_c^+/D^0 ratio at low multiplicity as a complement to EIC-BNL measurements. The measurement of the charm baryon-to-meson ratio can provide insight into the interplay between the hard and soft processes that produce particles. In pp or AA collisions, a higher charged particle multiplicity corresponds to higher collision energy and lower impact parameters. The events with different collision energies and impact parameters will have different underlying event structures. Thus, a wider coverage of multiplicity is necessary to study the charm hadronization at γ-nucleon and γ-nuclei collision systems.

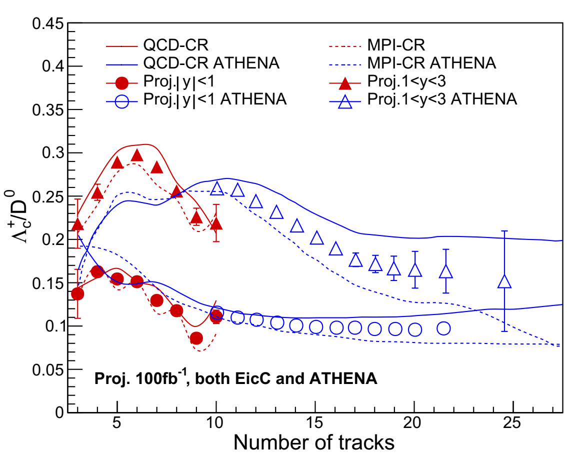

FIG. 11. The projection of the statistical uncertainty of Λ_c^+/D^0 ratio as a function of multiplicity. The description of both lines and points is similar to what has been discussed in Fig. 10. The red and blue points are for EicC results and ATHENA results [33].

B. D^0 double ratio

Hadron production is affected by initial and final state interactions. The primary initial effect is EMC effect, which is not of interest in this particular study. We focus on the final state interaction and the effect of the surrounding nuclear medium on hadronization. To minimize the initial state effect, the observable double ratio is defined as

$$R_{eA}^h(Q^2, x_B, z) = \frac{N_A^h(Q^2, x_B, z)/N_A^{\mathrm{DIS}}(Q^2, x_B)}{N_p^h(Q^2, x_B, z)/N_p^{\mathrm{DIS}}(Q^2, x_B)},$$

where N^{DIS} and N^h are the number of DIS electrons and the number of the semi-inclusive hadrons h, respectively.

DIS requirements, including (i) $Q^2 > 2$ GeV^2, (ii) $\nu < 96$ GeV, and (iii) $W^2 > 4$ GeV^2 are applied. The statistical uncertainty projection of D^0 double ratio as a function of z is shown in Fig. 12. Here, the electron-nucleus collision is the eAu collision with electron momentum 3.5 GeV$/c$ and Au momentum 12.93 GeV$/c/u$. The center values of all

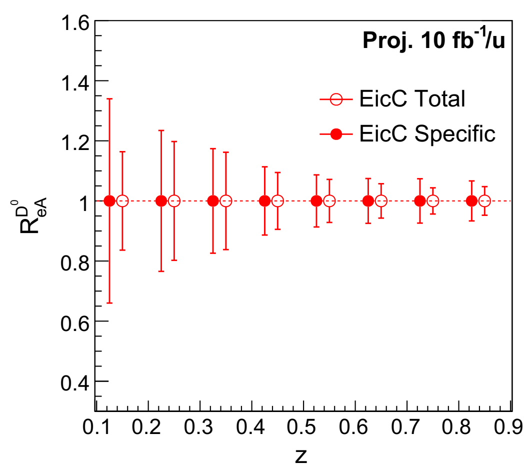

FIG. 12. The D^0 double ratio: The statistical uncertainty projections are corresponding to an integral luminosity $\mathcal{L}_{\mathrm{int}} = 10$ fb^{-1}. The open and solid circles represent the results of EicC total kinematic coverage (EicC total: 2 GeV^2 < Q^2 < 200 GeV^2, $\nu < 96$ GeV) and a smaller specific kinematic coverage (EicC specific: 2 GeV$^2 < Q^2 < 8$ GeV^2, 48 GeV $< \nu < 77$ GeV).

the points are set to 1 because there should be no medium modification in PYTHIA. The statistical uncertainty is scaled to the integral luminosity $10\ \mathrm{fb}^{-1}/u$ of electron-nucleus and electron-proton collision data. The open red circles are EicC results for the whole kinematic region. The solid red circles are EicC results for additional DIS criteria: $Q^2 < 8\ \mathrm{GeV}^2$ and $48\ \mathrm{GeV} < \nu < 77\ \mathrm{GeV}$. The EicC specific kinematic coverage in Fig. 12 is chosen to be a region, where ν is rather low and the D^0 are produced abundantly.

There are precise measurements of the light hadron double ratio ($\pi^{+/-}, K^{+/-}, p$ and $\bar{p}$) versus multiple variables at HERMES. However, as mentioned earlier, two theories with different time scales can adequately describe the HERMES data [20,34]. To provide an additional powerful constraint to these theories, D^0 double ratio is necessary because that D^0 double ratio is very different from that of light hadrons. For light hadrons, the values of the double ratio at $z > 0.05$ are below unity for nuclear attenuation or parton energy loss. However, for D^0, there is an enhancement of the ratio of $c \to D^0$ fragmentation function (FF) in medium to FF in vacuum at low z [35]. In the definition of the double ratio, the effect caused by the nuclear PDF and the hard scattering cross section is canceled by the DIS event number normalization. The effect remaining in the double ratio is caused by the FF ratio. So D^0 double ratio is higher than unity at low z bins and lower than unity at high z bins for the same reason as light hadron suppression. In addition, a lower c.m. energy can produce a larger cold nuclear effect [35]. Therefore, EicC, which has a lower c.m. energy than EIC-BNL but can abundantly produce D^0, can be an ideal facility to study how the nuclear medium affects the hadronization process. Additionally, it can complement EIC-BNL by covering a wider kinematic region.

IV. SUMMARY

In summary, open charm reconstruction is studied with fast simulation, where the detector performance parameterizations are derived from the Geant4 simulation with the developing detector geometry designed for EicC. The reconstruction of $D^0(\to K^-\pi^+)$ and $\Lambda_c^+(\to p\pi^+K^-)$ in the $\sqrt{s} = 16.7$ GeV ep collision demonstrates the importance of vertex detectors in reducing background and improving momentum resolutions. This leads to higher signal significance and lower statistical uncertainties, providing sufficient precision for future charm hadronization studies in EicC.

We have projected the statistical uncertainty of Λ_c^+/D^0 ratios as functions of p_T and charged-particle multiplicity. Different hadronization models (QCD-CR and MPI-CR) can be distinguished with the projected statistical uncertainties at an integrated luminosity of $\mathcal{L}_{\mathrm{int}} = 100\ \mathrm{fb}^{-1}$. A broader rapidity coverage than ALICE can provide abundant information about hadronization in γ-nucleon and γ-nuclei collision systems.

The statistical uncertainties of the double ratio of D^0, which behave differently from light hadron double ratios, are projected as a function of z at an integrated luminosity of $\mathcal{L}_{\mathrm{int}} = 10\ \mathrm{fb}^{-1}/\mathrm{u}$. Precise measurements at EicC can provide an excellent opportunity to understand charm hadronization mechanisms and how charm interacts with the nuclear medium.

ACKNOWLEDGMENTS

This work is supported in part by the Strategic Priority Research Program of the Chinese Academy of Sciences under Grant No. XDB34000000, the National Key R&D Program of China with Grants No. 2018YFE0104700 and No. 2018YFE0205200 and the National Natural Science Foundation of China with Grants No. 11890712, No. 12375141, No. 12061141008, the Guangdong Major Project of Basic and Applied Basic Research No. 2020B0301030008, the Guangdong Provincial Key Laboratory of Nuclear Science with Grant No. 2019B121203010. The authors acknowledge the computing resources available at the Southern Nuclear Science Computing Center.

[1] R. D. Ball *et al.* (NNPDF Collaboration), Parton distributions from high-precision collider data, Eur. Phys. J. C **77**, 663 (2017).

[2] J. J. Ethier and E. R. Nocera, Parton distributions in nucleons and nuclei, Annu. Rev. Nucl. Part. Sci. **70**, 43 (2020).

[3] A. Accardi *et al.*, Electron ion collider: The next QCD frontier: Understanding the glue that binds us all, Eur. Phys. J. A **52**, 268 (2016).

[4] R. Abdul Khalek *et al.*, Science requirements and detector concepts for the electron-ion collider: EIC Yellow report, Nucl. Phys. **A1026**, 122447 (2022).

[5] D. P. Anderle *et al.*, Electron-ion collider in China, Front. Phys. **16**, 64701 (2021).

[6] J. Arrington *et al.*, Physics with CEBAF at 12 GeV and future opportunities, Prog. Part. Nucl. Phys. **127**, 103985 (2022).

[7] B. Andersson, *The Lund Model*, Cambridge Monographs on Particle Physics, Nuclear Physics and Cosmology Vol. 7 (Cambridge University Press, Cambridge, England, 2023).

[8] R. J. Fries, V. Greco, and P. Sorensen, Coalescence models for hadron formation from quark gluon plasma, Annu. Rev. Nucl. Part. Sci. **58**, 177 (2008).

[9] S. Acharya *et al.* (ALICE Collaboration), Prompt D^0, D^+, and D^{*+} production in Pb–Pb collisions at $\sqrt{s_{NN}} = 5.02$ TeV, J. High Energy Phys. 01 (2022) 174.

[10] S. Radhakrishnan (STAR Collaboration), Measurements of open charm production in Au + Au collisions at $\sqrt{s_{NN}} = 200$ GeV with the STAR experiment at RHIC, Nucl. Phys. **A982**, 659 (2019).

[11] R. Aaij *et al.* (LHCb Collaboration), Study of prompt D^0 meson production in *p*Pb collisions at $\sqrt{s_{NN}} = 5$ TeV, J. High Energy Phys. 10 (2017) 090.

[12] S. Acharya *et al.* (ALICE Collaboration), Λ_c^+ production in pp collisions at $\sqrt{s} = 7$ TeV and in p-Pb collisions at $\sqrt{s_{NN}} = 5.02$ TeV, J. High Energy Phys. 04 (2018) 108.

[13] S. Acharya *et al.* (ALICE Collaboration), Constraining hadronization mechanisms with Λ_c^+/D^0 production ratios in Pb–Pb collisions at sNN = 5.02 TeV, Phys. Lett. B **839**, 137796 (2023).

[14] A. Beraudo, A. De Pace, M. Monteno, M. Nardi, and F. Prino, In-medium hadronization of heavy quarks and its effect on charmed meson and baryon distributions in heavy-ion collisions, Eur. Phys. J. C **82**, 607 (2022).

[15] H.-S. Shao, HELAC-Onia: An automatic matrix element generator for heavy quarkonium physics, Comput. Phys. Commun. **184**, 2562 (2013).

[16] A. Airapetian *et al.* (HERMES Collaboration), Hadronization in semi-inclusive deep-inelastic scattering on nuclei, Nucl. Phys. **B780**, 1 (2007).

[17] M. S. Abdallah *et al.* (STAR Collaboration), Disappearance of partonic collectivity in sNN = 3 GeV Au + Au collisions at RHIC, Phys. Lett. B **827**, 137003 (2022).

[18] *Properties of QCD Matter at High Baryon Density*, edited by X. Luo, Q. Wang, N. Xu, and P. Zhuang (Springer, New York, 2022).

[19] E.-C. Aschenauer *et al.* (RHIC SPIN Collaboration), The RHIC cold QCD program, arXiv:2302.00605.

[20] B. Z. Kopeliovich, J. Nemchik, E. Predazzi, and A. Hayashigaki, Nuclear hadronization: Within or without?, Nucl. Phys. **A740**, 211 (2004).

[21] S. Agostinelli *et al.* (GEANT4 Collaboration), Geant4–a simulation toolkit, Nucl. Instrum. Methods Phys. Res., Sect. A **506**, 250 (2003).

[22] T. Sjostrand, S. Mrenna, and P. Z. Skands, PYTHIA 6.4 physics and manual, J. High Energy Phys. 05 (2006) 026.

[23] PYTHIA 6.4.28, https://eic.github.io/software/pythia6.html, Last accessed on 2023-4-17.

[24] T. Sjostrand and P. Z. Skands, Multiple interactions and the structure of beam remnants, J. High Energy Phys. 03 (2004) 053.

[25] D. P. Anderle, A. Guo, F. Hekhorn, Y. Liang, Y. Ma, L. Xia, H. Xing, and Y. Zhao, Probing gluon distributions with D^0 production at the EicC, arXiv:2307.16135.

[26] S. Chekanov *et al.* (ZEUS Collaboration), Measurement of charm fragmentation ratios and fractions in photoproduction at HERA, Eur. Phys. J. C **44**, 351 (2005).

[27] H. Abramowicz *et al.* (ZEUS Collaboration), Measurement of D^+ and Λ_c^+ production in deep inelastic scattering at HERA, J. High Energy Phys. 11 (2010) 009.

[28] B. Abelev *et al.* (ALICE Collaboration), Measurement of charm production at central rapidity in proton-proton collisions at $\sqrt{s} = 2.76$ TeV, J. High Energy Phys. 07 (2012) 191.

[29] P. Avery *et al.* (CLEO Collaboration), Inclusive production of the charmed baryon Λ_c^+ from e^+e^- annihilations at $\sqrt{s} = 10.55$ GeV, Phys. Rev. D **43**, 3599 (1991).

[30] S. Acharya *et al.* (ALICE Collaboration), Λ_c^+ production and baryon-to-meson ratios in pp and p-Pb collisions at $\sqrt{s_{NN}} = 5.02$ TeV at the LHC, Phys. Rev. Lett. **127**, 202301 (2021).

[31] J. R. Christiansen and P. Z. Skands, String formation beyond leading colour, J. High Energy Phys. 08 (2015) 003.

[32] S. Acharya *et al.* (ALICE Collaboration), Charm-quark fragmentation fractions and production cross section at midrapidity in pp collisions at the LHC, Phys. Rev. D **105**, L011103 (2022).

[33] J. Adam *et al.* (ATHENA Collaboration), ATHENA detector proposal—a totally hermetic electron nucleus apparatus proposed for IP6 at the electron-ion collider, J. Instrum **17**, P10019 (2022).

[34] N.-B. Chang, W.-T. Deng, and X.-N. Wang, Initial conditions for the modified evolution of fragmentation functions in the nuclear medium, Phys. Rev. C **89**, 034911 (2014).

[35] H. T. Li, Z. L. Liu, and I. Vitev, Heavy meson tomography of cold nuclear matter at the electron-ion collider, Phys. Lett. B **816**, 136261 (2021).